Chemical Engineering Journal 475 (2023) 146209

Contents lists available at ScienceDirect

Chemical Engineering Journal

journal homepage: www.elsevier.com/locate/cej

Thermal and chemical durability of metal halide perovskite $CsPbBr_3$ single crystals

Daniu Han [a], Kun Yang [a,*], Chengying Bai [b], Feida Chen [a], Zhangjie Sun [a], Yibo Wang [a], Hao Ji [a], Zhou Yang [a], Xiaobin Tang [a,*]

[a] College of Materials Science and Technology, Nanjing University of Aeronautic and Astronautics, Jiangsu Province, 210016, PR China
[b] College of Materials Science and Chemical Engineering, Harbin Engineering University, Heilongjiang Province, 150001, PR China

ARTICLE INFO

Keywords:
Perovskite single crystal
Chemical durability
Non-congruent leaching

ABSTRACT

Halide perovskite $CsPbBr_3$ single crystals have shown promising applications in high-energy radiation detection because of their high gamma-ray blocking capability, strong hole carrier transport capability, and manufacturing feasibility. However, the soft ionic properties of perovskite octahedral lattice facilitate the phase transformation of $CsPbBr_3$ under a hydrothermal environment, which significantly limits their application. The current work systematically studied the phase stability of the $CsPbBr_3$ single crystals under high temperatures and high humidity to accelerate their potential application in high-energy radiation detection. Thermal and water degradation behaviors of the $CsPbBr_3$ single crystals under elevated temperature were investigated for the first time via in situ Raman spectroscopy and semi-dynamic leaching testing methods. Results indicated that the $CsPbBr_3$ single crystals exhibited good thermal stability below 460 °C without obvious phase degradation and rapidly transformed to $CsPb_2Br_5$, followed by PbBr(OH) with the continuous water interaction. The water interaction and phase degradation mechanism of single crystals with the preferential release of Cs, surface reorganization, and formation of PbBr(OH) alteration layer with rod-like structure was revealed. The phase degradation of $CsPbBr_3$ single crystals along surface defects from the growth process was further confirmed, which can be used to guide subsequent work on single-crystal stability regulation.

1. Introduction

The development and application of high-performance and long-life semiconductor materials have always been the concern of researchers in the field of modern nuclear radiation detection since the 1960 s [1]. At this stage, variable semiconductor materials, including gallium arsenide (GaAs), mercury iodide (HgI_2), and cadmium telluride (CdTe) [2], have been developed to meet the requirements of modern radiation detection, such as high sensitivity, high detection efficiency, and convenience [3]. However, those materials suffer from the disadvantages of high manufacturing cost [4], low stability, and ready to decomposition [5].

Halide perovskite single crystals have shown broad application prospects in solar cells, light-emitting diodes, and radiation detectors because of their simple preparation process, excellent carrier transport properties, and surprisingly high defect tolerance [6–10]. Currently, the widely studied halide perovskite materials are mainly focused on Pb-based halide perovskites, which contain heavy ions of Pb, making them effective at blocking high-energy radiation; the abundant energy level structure of Pb ions greatly enhances the charge transport capability of the materials [11]. Existing studies showed that organic–inorganic hybrid perovskite $MAPbBr_3$ and $FAPbBr_3$ single crystals with organic functional group cations MA^+ and FA^+ at the A-position have high electronic quality [12,13], with their photoelectric conversion efficiency exceeding 22% [14,15]. However, the readily volatile MA^+ results in rapid thermal decomposition at relatively low temperatures, whereas the strong polarization of MA^+ raises the issue of ion migration [16,17], which is not favorable for long-term stable applications. Compared with hybrid perovskites, the substitution of organic cations by the inorganic metal cation Cs^+ to form $CsPbBr_3$ single crystals increases the structural stability [18,19], with a large band gap of 2.3 eV and a large average atomic number (effective atomic number Z_{eff} of 65.9, which is much higher than that of CdZnTe (50.2)) [20]. He et al. [21] enabled a $CsPbBr_3$ single-crystal semiconductor detector to achieve a remarkable energy resolution of 1.4 % for ^{137}Cs by improving the

* Corresponding authors.
E-mail addresses: kun.yang@nuaa.edu.cn (K. Yang), tangxiaobin@nuaa.edu.cn (X. Tang).

https://doi.org/10.1016/j.cej.2023.146209
Received 28 July 2023; Received in revised form 12 September 2023; Accepted 20 September 2023
Available online 24 September 2023

electrode structure design and preparation process.

Although the $CsPbBr_3$ single crystal exhibits promising application in radiation detectors, the inherent soft ionic property of its crystalline structure makes $CsPbBr_3$ single crystals unfavorable for use in high-humidity environments [22]. As a result, the environmental degradation and elemental release of Pb-based halide perovskites have received increasing attention. Caddeo et al. [23] studied the water-caused perovskite $MAPbI_3$ degradation mechanism and obtained a collective water dissolution mechanism in which MA^+ ions are removed from the lattice in 10 ps. This MA^+ ion dissolution time was even faster at 8.5 ps in the study by Mosconi et al. [24]. Bryce et al. [25] experimentally investigated the chemical durability and degradation mechanisms of $CsPbI_3$ polycrystalline perovskite in aqueous environments and found that both I and Cs ions exhibit incongruent leaching behavior with a release rate faster than Pb, especially under long leaching times and high temperatures. Zhang et al. [26] simulated the spontaneous dissolution process of $CsPbI_3$ in water, and they deduced that the large hydration enthalpy of $CsPbI_3$ together with the low lattice energy of the perovskite structure may be responsible for the rapid release of Cs^+ and the fast degradation of $CsPbI_3$ in water. Although numerous studies on the Pb halide perovskite stability are based on the polycrystalline structure, few studies have focused on the degradation behavior toward the single crystal despite the fact that the single crystal has demonstrated superior photovoltaic behavior due to the disappearance of the defect [27]. In particular, studies on the water degradation of $CsPbBr_3$ single crystals are rare.

In the current study, $CsPbBr_3$ single crystal was successfully synthesized through a water-based anti-solvent vapor-assisted method. The thermal and chemical durability of the single crystal was systematically studied via in-situ Raman and semi-dynamic leaching tests. The phase degradation pathway and microstructure evolution of single crystals in deionized water were further revealed through scanning electron microscopy–energy dispersive spectroscopy (SEM-EDS), X-ray diffraction (XRD), Raman spectroscopy. The elemental release rate of the single crystal was revealed by induced couple plasma–mass spectroscopy (ICP-MS) to elucidate the underlying dissolution behavior and achieve a mechanistic understanding of corrosion and surface reorganization.

2. Materials and methods

2.1. Single-crystal preparation

The $CsPbBr_3$ single crystal was synthesized by an anti-solvent vapor-assisted method [28,29], which is shown in Fig. 1a. CsBr (Macklin, 99.9%) and $PbBr_2$ (Macklin, 99.0%) with a molar ratio of 1:1.5 were dissolved in 15 mL of dimethyl sulfoxide (DMSO, Macklin. GC, $\geq$ 99.8%) to configure a pure $CsPbBr_3$ phase solution with a concentration of 0.4 mol $\cdot$ L^{-1} (Cs concentration of 0.4 mol $\cdot$ L^{-1}) [29], followed by stirring at 60 °C for 0.5 h until the solution was clear. The solution was then titrated with 5 mL of methanol (MeOH, Nanjing Chemical Industry Co. AR, $\geq$ 99.8%) until an insoluble yellow $CsPbBr_3$ precipitate appeared in the beaker. The precipitate was further removed with polytetrafluoroethylene (PTFE) 0.1 μm pore-size filter paper, leaving a saturated precursor solution. About 30 mL of dilute methanol anti-solvent was made by equally mixing 10.9 mL MeOH with 19.1 mL DMSO in a molar ratio of 1:1. The beaker containing $CsPbBr_3$ saturated precursor solution was placed in a large beaker with diluted methanol anti-solvent at 40 °C for 3 days to obtain a number of single crystals with a size of 1–4 mm, as shown in Fig. 1a. Large single crystals (~4 mm) were further grown from the $CsPbBr_3$ seeds following the seed crystal method [30], in which the seed crystals with regular shapes and large sizes were selected as nucleation sites to assist single-crystal growth and further increase the single crystal size.

2.2. Single-crystal phase and micro-structural characterization

Crystalline phase property of the single crystal before and after the leaching test was evaluated by XRD (PAN analytical, the NL) with a PIXcel3D array detector receiver and a copper target for ray characterization (scan ranged from 10° to 70° with a scanning speed of 0.094° $\cdot$ s^{-1}); the microstructure evolution before and after the leaching test was determined by using a double ionization beam (SEM/FIB) electron microscope (TESCAN LYRA3 GM, CZ) equipped with an EDS system (Oxford system, the UK).

2.3. Thermal stability

The thermal stability of the single crystal was evaluated by TGA-DSC (STA 449 F3, GER) with a temperature range from 25 °C to 1000 °C and a temperature ramping rate of 10 °C $\cdot$ min^{-1} in argon atmosphere. The crystalline phase evolution was further characterized by in situ Raman spectroscopy under air atmosphere using a high-resolution Raman spectrometer (HORIBA HR Evolution, FR) with an excitation wavelength of 633 nm. The temperature was dynamically controlled by a heating stage (Linkam, the UK) with a heating rate of 5 °C $\cdot$ min^{-1} from 10 °C to 460 °C.

2.4. Dissolution experiment

A semi-dynamic leaching test [31] (ASTM C1308) was conducted to

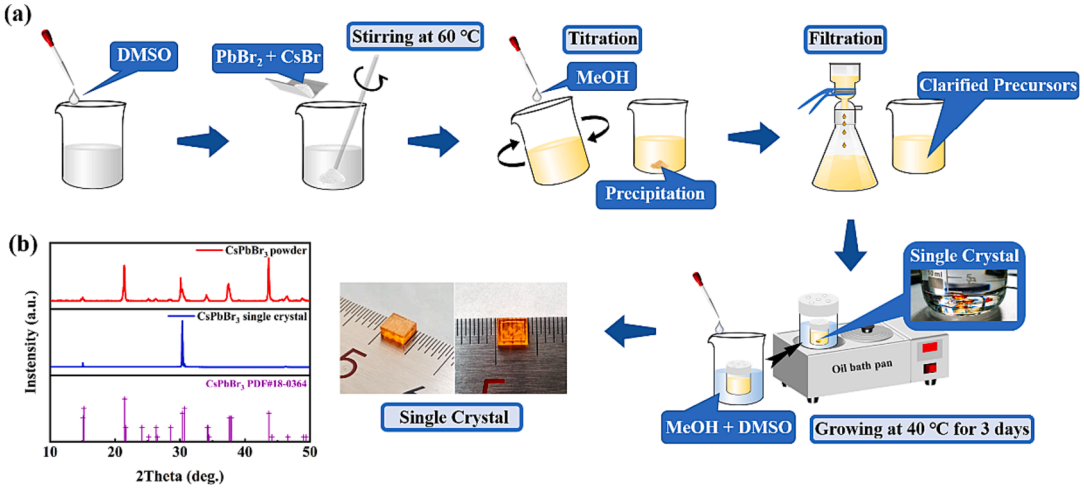

Fig. 1. (a) Anti-solvent vapor-assisted crystallization and optical view of the $CsPbBr_3$ single crystals; (b) X-ray diffraction pattern of the $CsPbBr_3$ single crystals.

characterize the chemical stability of the $CsPbBr_3$ single crystals to understand the phase degradation behavior and dissolution kinetics. Specifically, the sample was immersed in a PTFE vial with deionized water for a given time interval, and the leachate was periodically replaced with new leachate after each time interval. The semi-dynamic leaching test was performed under three different temperature ranges from 20 °C, 59 °C, and 90 °C. The Cs, Pb, and Br concentrations in leachate were then diluted 100 times and analyzed with an inductively coupled plasma-mass spectrometry (ICP-MS) system (ICAP6300, US) to obtain the time-dependent dissolution amounts of the three elements. The corresponding release rate $m(i)$ of each element (in $mg \cdot m^{-2} \cdot d^{-1}$), as well as elemental dissolution control rate constant k_1 and diffusion control rate constant k_2, was calculated by the method proposed by Yang et al. [31]. The elemental dissolution activation energy E_a (in $kJ \cdot mol^{-1}$) associated with the dissolution mechanism of each element was further obtained by calculating the Arrhenius equation according to Bryce et al. [25].

3. Characterization of $CsPbBr_3$ single crystals

3.1. Phase and microstructure

The XRD profiles of the prepared $CsPbBr_3$ single crystals shown in Fig. 1b demonstrated a high-purity meritocratic orientation with characteristic peaks at 15.03°, 30.37°, and 46.24°, belonging to the single crystalline orientations of (001), (002), and (003), respectively. The XRD characterization also revealed that the single crystals belonged to the orthorhombic structure. The surface microstructure of the $CsPbBr_3$ single crystals is shown in Fig. 2. The lamellar growth morphology of single crystals followed the crystal lamellar growth theory (Kossel-Stransky theory) [32], where a single crystal grew stepwise like a reversed pyramid from one stage to another, thereby forming a multilayer lamellar structure (Fig. 2a-d). The elemental mappings and corresponding semi-quantitative analysis on the surface of the $CsPbBr_3$ single crystal indicated the uniform distribution of the three elements (Cs, Pb, and Br) on the surface with the elemental ratio close to 1:1:3 (Fig. 2e-h).

3.2. Thermodynamic stability

The temperature-dependent thermal weight loss curves and the DSC curves of the $CsPbBr_3$ single crystal are shown in Fig. 3a, b, respectively. A sharp DSC absorption peak was found at 567.9 °C (Fig. 3b), which was consistent with previous reports and implied a melting point at 567.9 °C [33]. Before 580 °C, the heat loss curve exhibited a plateau (Fig. 3a), indicating minimal weight loss in the single crystal, probably due to the remaining organic solvent. The heat weight loss curve, as well as two successive decreases for the DSC curve (starting at 580 °C and 900 °C, respectively), may be attributed to the thermal decomposition of the single crystal, which experienced two distinct scenarios, namely, the decomposition reaction of $PbBr_2$ started at about 500 °C [34,35], and CsBr sublimated at about 800 °C [36,37]. The decomposition temperatures of $PbBr_2$ and CsBr were slightly higher than those in previous reports [35,36], indicating the enhancement of thermal stability by forming a single crystal.

The thermal stability of the $CsPbBr_3$ single crystal was further studied by in-situ Raman spectroscopy from 10 °C to 580 °C with a 633 nm laser as the excitation source at a temperature interval of 50 °C (Fig. 3c). The Raman spectra of the $CsPbBr_3$ single crystal were composed of three active Raman vibrations concentrated at 76, 135, and 311 cm^{-1} [13,38]. The central peak at 76 cm^{-1} corresponded to the phonon vibration mode of TO_2, which was related to the motion of Cs^+ and the vibration of $[PbBr_6]^{4-}$ [13], whereas the broad low-intensity peak around 135 cm^{-1} corresponded to the phonon vibration mode of TO_3, which was mainly related to the motion of Cs ions [38]. The peak at 311 cm^{-1} was related to the Raman second-order phonon scattering mode of $CsPbBr_3$ [38–40]. The result of in situ Raman spectra test revealed that the three characteristic peaks of $CsPbBr_3$ gradually shifted to a high angle (red-shift) as well as broadened with increasing temperature from 10 °C, which could be attributed to the stress–strain formed by the lattice distortion derived from the volume expansion of the single crystal upon heating [38,41]. No obvious new peaks could be found for the current temperature range (from 10 °C to 460 °C) as evidenced by the current Raman spectra, which meant that the single crystal had not decomposed. Previous work showed that the all-inorganic perovskite $CsPbBr_3$ with inorganic metal cation Cs^+ at the A-site has excellent thermal stability compared with the organic–inorganic hybrid perovskite $MA\text{-}PbX_3$ [30,42], which was also verified in the current work. We observed the good thermal stability of $CsPbBr_3$ single crystals below 460 °C. The corresponding optical micrographs in Fig. 3d demonstrated the ripple-like morphology on the surface of a single crystal from 310 °C, which became more obvious by elevating the temperature. This result suggested that the $CsPbBr_3$ single crystal started to melt and transformed to the molten state at 310 °C. Therefore, temperatures above 310 °C were not favorable for the application of bulk $CsPbBr_3$ single crystal.

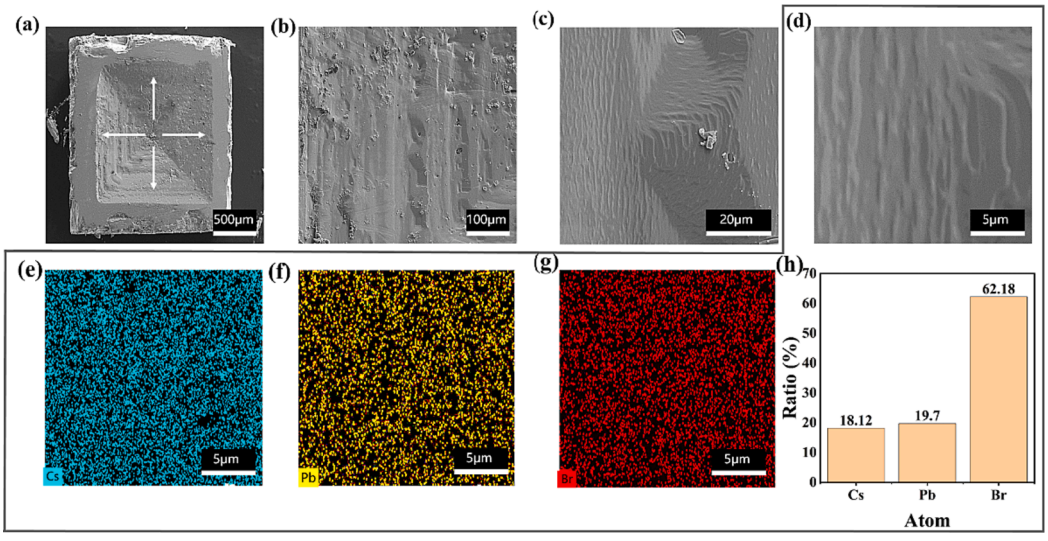

Fig. 2. SEM morphology of $CsPbBr_3$ single crystal: (a-d) surface morphology of $CsPbBr_3$ single-crystal sheet structure with magnification from 80 to 10 k times; (e-h) EDS mappings of $CsPbBr_3$ single-crystal sheet structure from Fig. 2d.

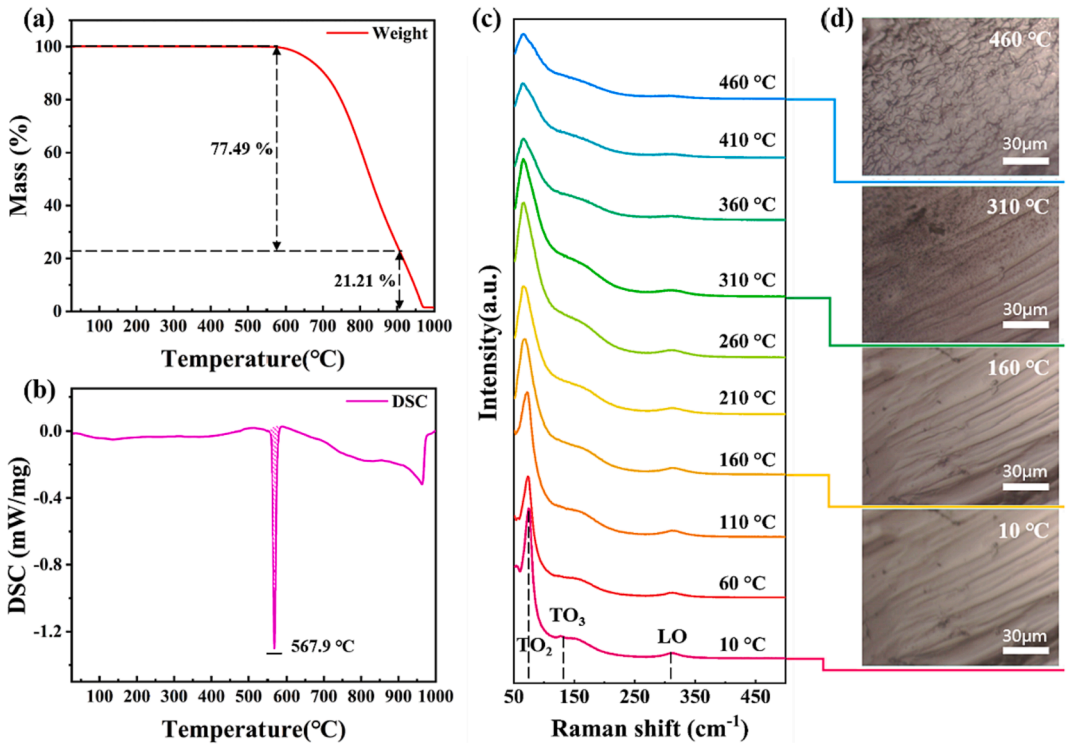

Fig. 3. (a) Thermal weight loss curve of $CsPbBr_3$ single crystals; (b) $CsPbBr_3$ DSC curve; (c) In situ Raman spectra of $CsPbBr_3$ single crystals (at 50 °C temperature intervals); (d) Optical microscopy images at corresponding temperatures.

4. Chemical durability of $CsPbBr_3$ single crystal

4.1. Crystalline structure evolution

The crystalline structural evolution of the $CsPbBr_3$ single crystal after water interaction was analyzed, and the XRD and Raman spectral characterization results of the single crystal are shown in Fig. 4. The XRD profiles of $CsPbBr_3$ single crystals post-water interaction at 20 °C for 0.5, 6, and 24 h are shown in Fig. 4a. The characteristic peaks of $CsPbBr_3$ that were diminished with $CsPb_2Br_5$ (23.35°, 29.35°, 33.34°, 35.44°, 37.90°, and 47.86°) appeared after the reaction for 0.5 h at 20 °C, demonstrating the phase degradation of $CsPbBr_3$ in aqueous and oxygen environments. The complete decomposition of $CsPbBr_3$ into $CsPb_2Br_5$ occurred by extending the time to 6 h, and the characteristic peaks of PbBr(OH) (17.73°, 21.45°, 29.34°, and 30.06°) and PbO (29.81°) appeared at 24 h, which could be attributed to the further decomposition of the $CsPb_2Br_5$ phase. The characteristic peak at 30.37° was greatly weakened at 59 °C compared with the peak intensity of the sample at 20 °C for $CsPbBr_3$ (Fig. 4b) and further disappeared at 90 °C, indicating that the phase degradation process was thermodynamically driven.

The Raman spectra of the sample post-leaching test at 20 °C for 0.5–24 h are shown in Fig. 4c. The $CsPbBr_3$ characteristic peaks of 76, 135, and 311 cm^{-1} diminished but replaced by the Raman peaks of $CsPb_2Br_5$ at 70 (belongs to B_{2g} phonon vibration mode), 77 (B_{1g}), and 132 cm^{-1} (A_{1g}) at 6 h, which confirmed the decomposition of $CsPbBr_3$ into $CsPb_2Br_5$; these findings were consistent with the XRD results [43,44]. New characteristic peaks were found at 90 cm^{-1}, which belonged to the phonon vibration mode of Ag associated with the orthogonal phase PbO, indicating the formation of PbO in the 24 h eroded sample [45,46], and at 262 and 325 cm^{-1}, belonging to the Ag phonon vibration mode, which was attributed to the vibration of the $PbOH^+$ integral stacking band [47] (the latter two peaks are shown in Fig. 4c1). In the Raman spectroscopic study by Reid et al. [45] for the Pb, KCl, and H_2O corrosion system, the 108 cm^{-1} Raman peak was attributed to the vibration of the $PbOH^+$ band, which was due to the phase degradation and formation of the PbCl(OH) phase. Considering the similarity between PbCl(OH) and PbBr(OH), we assumed that the 108 cm^{-1} characteristic peak in the Raman spectrum of the 24 h sample was due to the formation of the PbBr(OH) phase.

The optical microscopy images of the sample surface post-phase degradation at different stages are shown in Fig. S1 (supplementary material), which clearly indicated a rod-like crystalline structure of the sample surface at 20 °C for 24 h, consistent with the microscopic morphology of PbBr(OH) [48,49]. These results further suggested that the rod-like crystallization was the recrystallization product of the single crystal surface. The water-induced phase decomposition pathway could then be summarized in the sub-sequential chemical equations (1–4) below.

$$2CsPbBr_3 + H_2O \rightarrow CsBr + CsPb_2Br_5 + H_2O \quad (1)$$

$$CsPb_2Br_5 + H_2O \rightarrow CsBr + 2PbBr_2 + H_2O \quad (2)$$

$$PbBr_2 + H_2O \rightarrow PbBr(OH)\downarrow + HBr \quad (3)$$

$$PbBr(OH) \rightarrow PbO + HBr \quad (4)$$

Initially, $CsPbBr_3$ interacts with water molecules and decomposes into CsBr and $CsPb_2Br_5$ (Eq. (1)), followed by decomposition into CsBr and $PbBr_2$ (Eq. (2)), in which CsBr is readily dissolved in solution. Meanwhile, the hydration of $PbBr_2$ leads to the formation of PbBr(OH), which is recrystallized on the surface of the single crystal (Eq. (3)). Further dehydration of PbBr(OH) results in PbO (Eq. (4)), which is evidenced by the Raman and XRD profiles (Fig. 4). Similar degradation phenomena could also be observed for the sample etched at 90 °C for 0.5 h, suggesting that degradation behavior was thermodynamically driven (Fig. 4d, d1). On the other hand, the absence of $CsPbBr_3$ Raman peaks between 220 and 360 cm^{-1} for the Raman spectra of single crystal post leaching test at 59 °C for 0.5 h in Fig. 4d has been attributed to the different sampling scale between Raman spectra and XRD. The XRD is a wide-angle scanning technique, which interacts with the entire single crystal, while Raman laser beam is point-scanning, with a spot area of

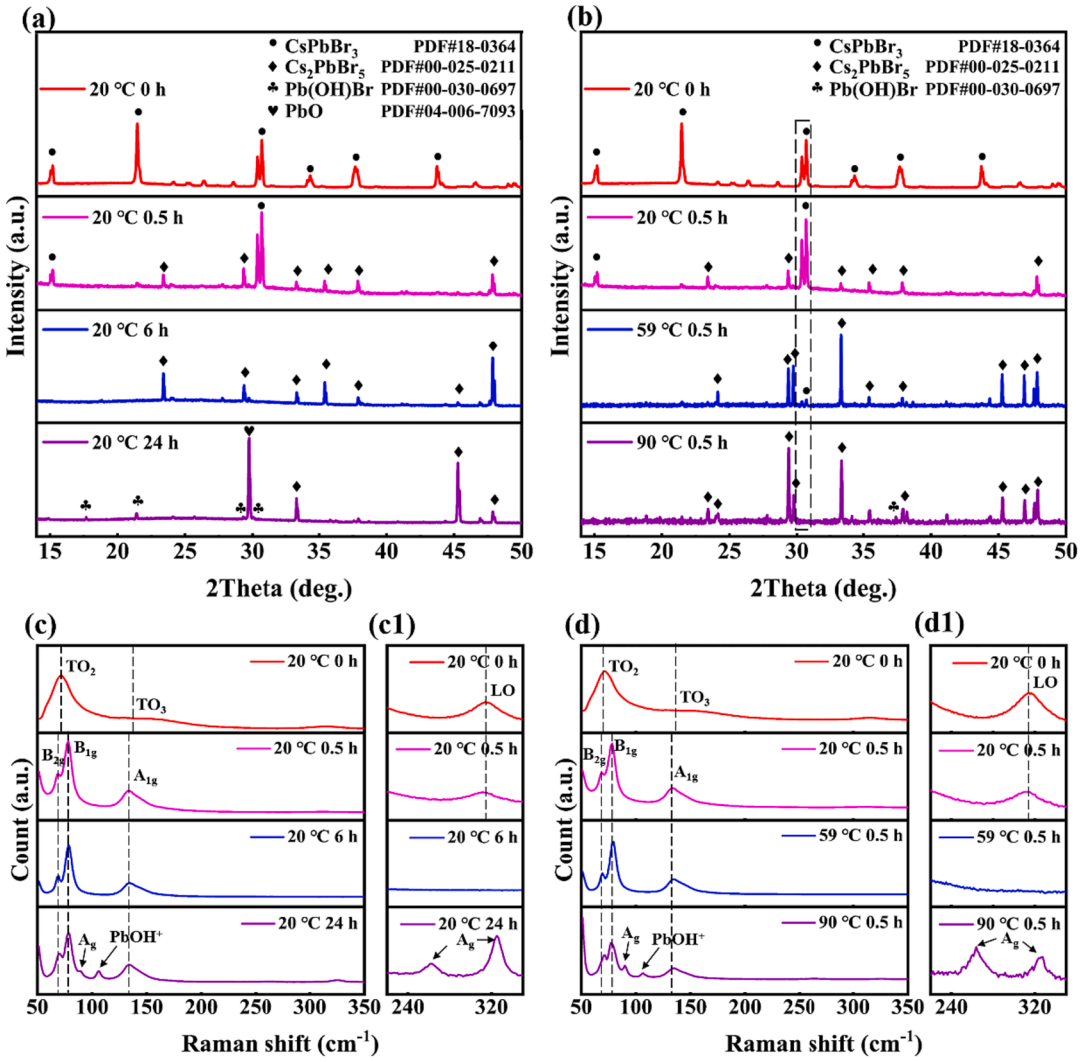

Fig. 4. X-ray diffraction spectra and Raman spectra of single-crystal degradation in deionized water with variable temperature and time: (a) time-dependent X-ray diffraction patterns after leaching at 20 °C; (b) X-ray diffraction patterns after leaching at 20 °C, 59 °C, and 90 °C for 0.5 h; (c) time-dependent Raman spectra at 20 °C; (c1) 220–360 cm^{-1} amplified spectra; (d) Raman spectra after leaching at 20 °C, 59 °C, and 90 °C for 0.5 h; (d1) 220–360 cm^{-1} amplified spectra.

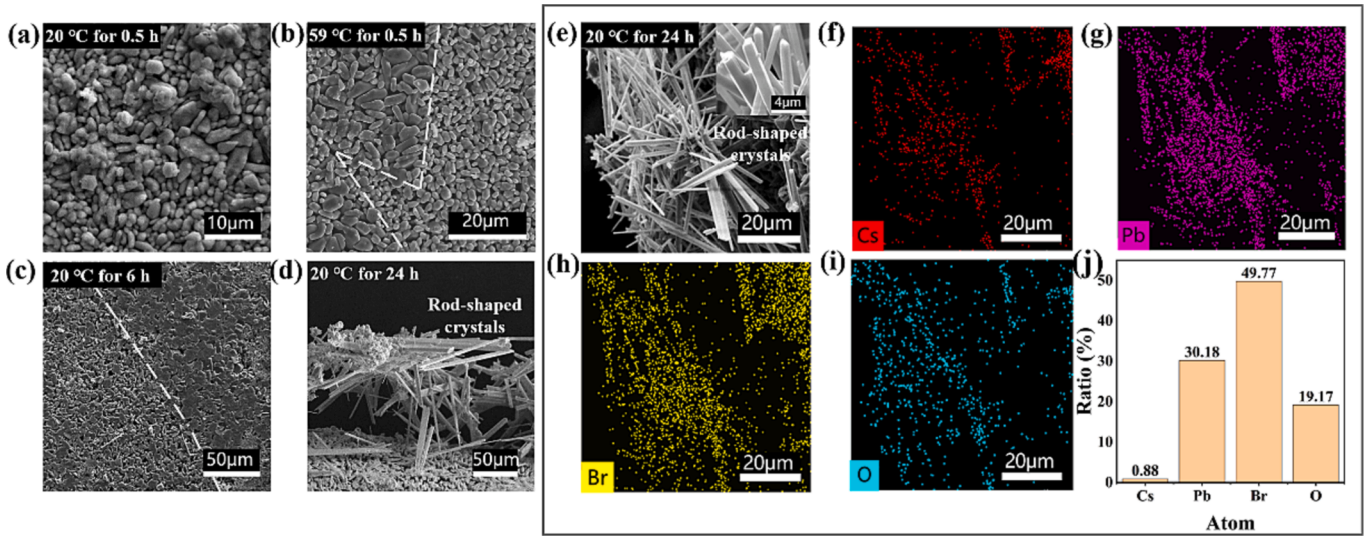

Fig. 5. Surface microstructure morphology of $CsPbBr_3$ single crystal after the leaching test: (a) 20 °C for 0.5 h; (b) 59 °C for 0.5 h; (c) 20 °C for 6 h; (d) 20 °C for 24 h; (e) rod-like crystal byproduct lay on the surface; (f-j) EDS data of rod crystal from Fig. 5e.

only 1.54 μm square, thus results in the absence of $CsPbBr_3$ Raman peaks in the 220–360 cm^{-1} range.

4.2. Microstructure evolution

The water-induced microstructure evolution of the $CsPbBr_3$ single crystal resulted in a large number of ellipsoidal particles packed on the surface for 0.5 h (Fig. 5a, b). With the intensification of corrosion, the corrosion-induced cavities between alteration products nearby continuously grew and expanded from 6 h to 24 h (Fig. 5c, d). Besides, numerous needle-like phase degradation products (Fig. 5d, e) were loosely packed on the single crystal surface, consistent with the results of optical microscopy in Fig. S1 (supplementary material). Elemental analysis on the needle-like alteration product demonstrated that the product was Cs-free and enriched with O, Pb, and Br, thereby indicating that it was a mixture of the hydrate PbBr(OH), PbO, and $PbBr_2$, originating from the decomposition of $CsPb_2Br_5$ to PbBr(OH) based on the previous results of XRD characterization. Fig. 5b, c show that the non-uniform feature of the water corrosion regions on the surface (bounded by the white dashed lines) might be ascribed to the presence of surface defects in these regions, which were generated by the single crystal growth. In these places, vacated ionic bonds were susceptible to water and oxygen and decomposed first, and the related arguments were proven by the results of the leaching experiments, which will be discussed in subsequent sections.

The cross-section microstructure and elemental distribution of the alteration layer corroded for 0.5 h at 20 °C are shown in Fig. 6a-e, and compared to the $CsPbBr_3$ single crystal before the leaching test (Fig. S2). The results show that the uncorroded single-crystal profile presents a good single-crystal step-like morphology and uniform elemental distribution. Compare to the single crystal before leaching test, the water-induced phase degradation of the single crystal started from the surface and gradually penetrated into the interior of the matrix with the thickness of the alteration layer around 600 μm within 0.5 h (Fig. 6a). The alteration layer from the top down to the center of the matrix could be divided into three distinct layers, namely, corroded layer, transition layer, and uncorroded layer (Fig. 6b). The morphology of the corroded layer showed a sheet-like structure with different length, and the transition layer showed the characteristics of pitting corrosion starting from the edge and center, whereas the uncorroded matrix still maintained the features of a $CsPbBr_3$ single crystal. A distinguishable interface was noted between the top corrosion layer and the transitional layer with a weak Cs signal in the corrosion layer, which suggested that the corrosion mechanism might be dominated by the stripping of Cs element at the early stage of corrosion based on the elemental maps (Fig. 6c-e). The increase in the proportion of Cs element for 0.5 h at 20 °C (Fig. 6f) may be due to the aggregation behavior of Cs stripping from the substrate. In addition, we inferred that the pitting corrosion morphology in the transition zone was due to a small amount of Cs stripping, and the pitting corrosion morphology will expand into the sheet-like crystal layer morphology with the intensification of corrosion.

The cross-sectional morphology of the single crystal post-leaching under high temperatures and long-term regimes is shown in Fig. 6g, h. The temperature-driven pitting corrosion with a similar sheet-like structure for the alteration layer post-leaching test (59 °C) is shown in Fig. 6g. The sheet-like structure converted to rod-like crystallization structure as corrosion increased by comparing the cross-section morphology of the samples at 0.5 and 24 h after the leaching test (Fig. 6b, h). Elemental mapping on the cross-section of the sample at 24 h post-leaching test indicated a partial Cs-depleted structure with an atomic ratio of Cs:Pb close to 1:2.2, further implying that the $CsPbBr_3$ structure was no longer present under this scenario (Fig. 6i-k, f). Considering the needle-like alteration product shown in Fig. 5d, e, we could reasonably assume that the continuous phase degradation of $CsPb_2Br_5$, which was derived from the early phase degradation of $CsPbBr_3$ with the release of Cs from the matrix, resulted in the alteration products of $PbBr_2$ and PbBr(OH) precipitate on the surface.

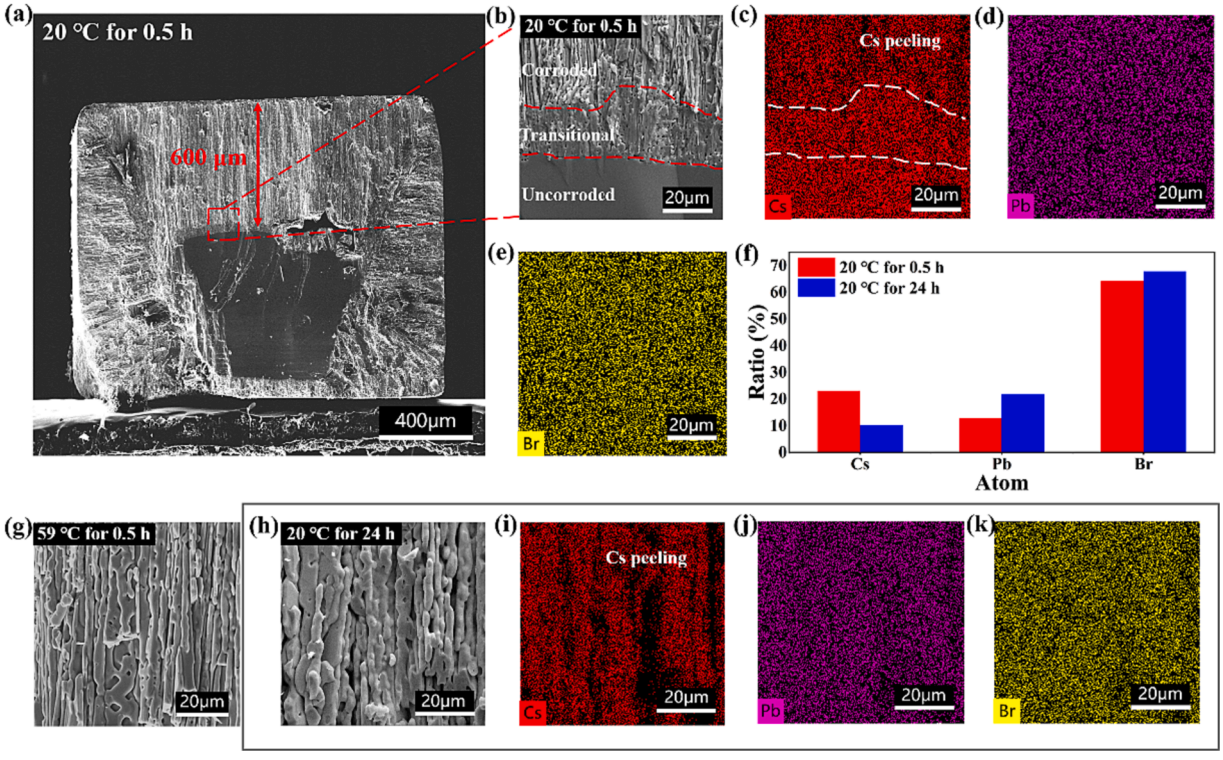

Fig. 6. Cross-sectional morphology of $CsPbBr_3$ single crystal after the leaching test: (a) 20 °C for 0.5 h; (b) the alteration layer from Fig. 6a; (c–e) EDS data of the alteration layer from Fig. 6b; (f) EDS quantitative results from Fig. 6b and Fig. 6h; (g) 59 °C for 0.5 h; (h) 20 °C for 24 h; (i-k) EDS result of the corrosion morphology from Fig. 6h.

4.3. Dissolution behavior and kinetics

The time-resolved dissolution curves for each element are shown in Fig. 7a-c. The dissolution behavior of $CsPbBr_3$ could be divided into two distinguishable regions, including an initial stage, which showed a leaching rate plateau and a gradual decreasing stage controlled by the diffusion mechanism (Fig. 7b, c), consistent with ceramic corrosion transition state theory [50]. However, the rapid release rate of Cs and Br elements at the early stage of corrosion (0.5 h) at 20 °C (Fig. 7a) could be attributed to the surface defects of single crystals [51,52]. The high surface energy and chemical inhomogeneity of these defects led to the rapid release of Cs element, which was evidenced by our previous SEM analysis (Fig. 5b, c), from which we demonstrated inhomogeneous corrosion of the single crystal surface. The elemental release rate of Cs is higher than that of Br and Pb. Pb element demonstrated the lowest elemental release rate among the three temperatures at the early stage of corrosion (0.5 h), as confirmed by Fig. 7a-c. The rapid release of Cs and Br elements at the early stage of corrosion under three temperatures with elemental depletion observed by the SEM images could be related to the weak Cs-Br ionic bond's breakage [25]. The elemental release rate of all three elements increased and reached the leaching equilibrium state faster with high temperatures, indicating that the elemental release and the transition of dissolution mechanisms from the initial non-stationary leaching to the final equilibrium leaching of the elements was thermodynamically driven.

The non-congruent leaching mechanism dominated the elemental release behavior of the three elements, as denoted by the atomic ratio in Fig. 7d-f. Specifically, the atomic ratio of Cs/Pb above 1.0 under three temperatures was at the early stage of corrosion (0.5 h) and gradually reduced below 1.0 with a final atomic ratio close to 0.5 at 32 h, which

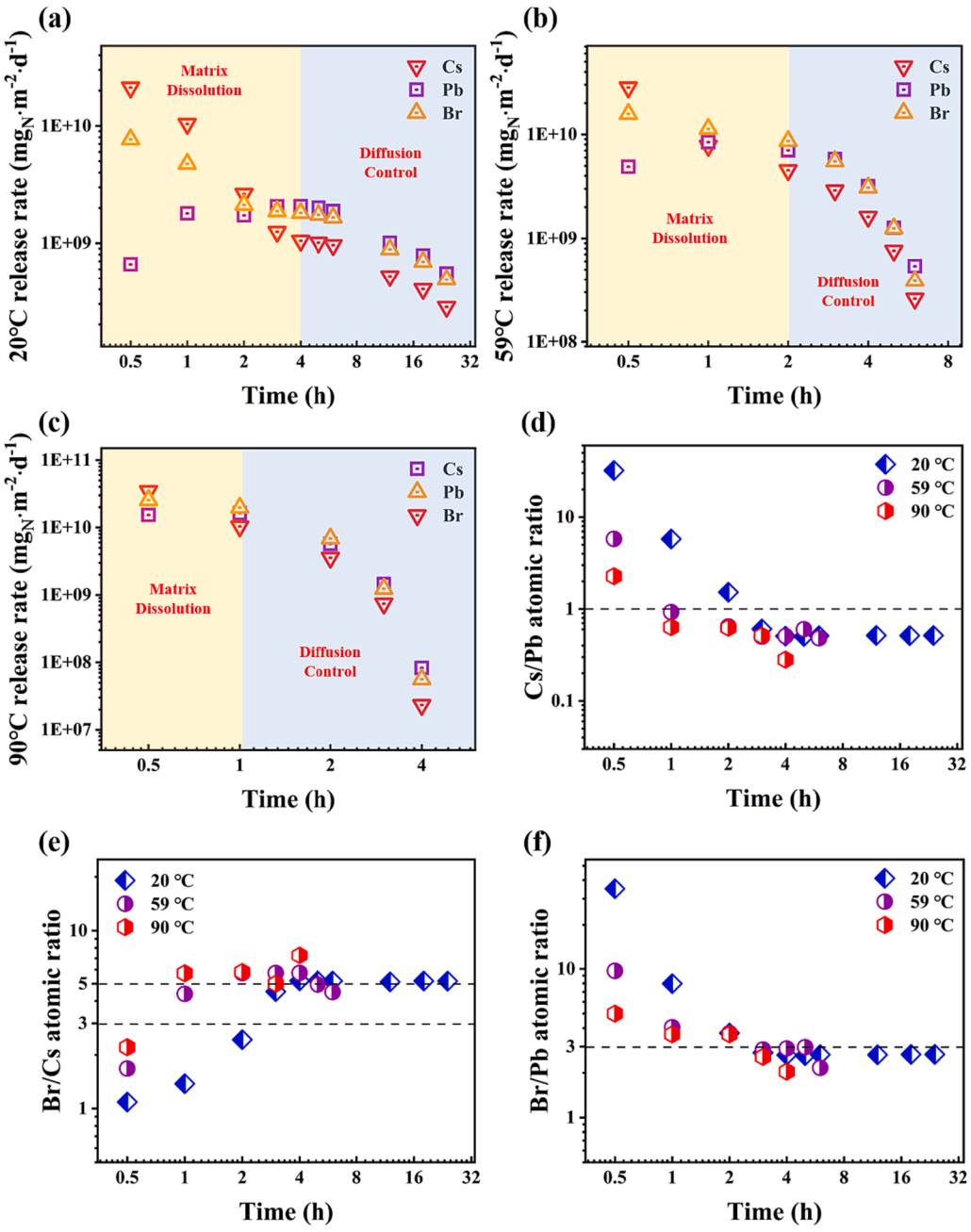

Fig. 7. Elemental release rate curves at various temperatures: (a) 20 °C; (b) 59 °C; (c) 90 °C; (d) Various atomic ratios (Cs/Pb (e) Br/Cs (f) Br/Pb) at 20 °C, 59 °C, and 90 °C.

was consistent with the Cs/Pb atomic ratio of $CsPb_2Br_5$. These results were consistent with the analysis of the XRD profiles in Fig. 4. The atomic ratio transition point was reached early by elevating the temperature from 20 °C to 90 °C, consistent with the XRD analysis, and this result confirmed that the degradation of $CsPbBr_3$ to $CsPb_2Br_5$ was thermodynamically driven. Moreover, the molar ratio for Br/Pb (5:2) and Br/Cs (5:1) was observed at 10 h, in accordance with $CsPb_2Br_5$ and the leaching mechanism transition from non-congruent to congruent.

The elemental cumulative dissolution curves with time are shown in Fig. 8a-c, which were further fitted by Cote's model [53], from which the corresponding dissolution control rate constants k_1 and diffusion control rate constants k_2 were obtained (Table 1). The dissolution free energy E_a of the three elements was further obtained by fitting the dissolution rate control constant k_1 versus the inverse of temperature with the Arrhenius equation [54] (as shown in Fig. 8d and Table 2). Cs element had the lowest dissolution free energy E_a with a value of 14.04 kJ•mol^{-1}, which demonstrated the preferential release of Cs ion. The low dissolution activation energy of Cs ion and favorable release of Cs could be further attributed to the weak Cs-Br chemical bond [55]. Pb had the highest dissolution activation energy of 28.36 kJ•mol^{-1}, which was the main reason for the slowest leaching rate of Pb ions during the leaching test of the single crystal. The high dissolution activation energy of Pb ions may be related to the strong bonding energy of Pb-Br ionic bonds [55]. The dissolution rate constants of Cs at all three temperatures were higher than the diffusion rate constants of Cs, which suggested that the release of Cs was mainly controlled by the dissolution process. By contrast, the diffusion rate constants of Pb and Br ions were greater than the dissolution rate constants, suggesting a diffusion-controlled elemental leaching mechanism for both elements at a low temperature of 20 °C. However, the dissolution rate constants of both elements exceeded the diffusion rate constants at elevated temperatures, further suggesting that the dissolution of $CsPbBr_3$ single crystals was a thermodynamically driven process.

Table 1
Dissolution control rate constant k_1 and diffusion control rate constant k_2 (in 10^8 $mg_N \cdot m^{-2} \cdot h^{-1}$) for each element fitted to Cote's equation.

Atom	Fitting parameters ($\times 10^8$ $mg_N \cdot m^{-2} \cdot h^{-1}$)	20 °C	59 °C	90 °C
Cs	k_1	3.04	5.64	9.39
	k_2	1.31	2.23	1.80
Pb	k_1	0.69	2.83	6.59
	k_2	2.56	4.32	3.04
Br	k_1	1.52	4.97	9.41
	k_2	2.25	4.12	3.39

Table 2
Dissolution activation energy E_a for each element according to the Arrhenius equation (in kJ · mol^{-1}).

	Dissolution
Activation energy	kJ · mol^{-1}
Cs	14.04
Pb	28.36
Br	23.04

5. Discussion

Compared with polycrystals, the single crystal structure maintains a regular crystal arrangement between ions rather than disordered

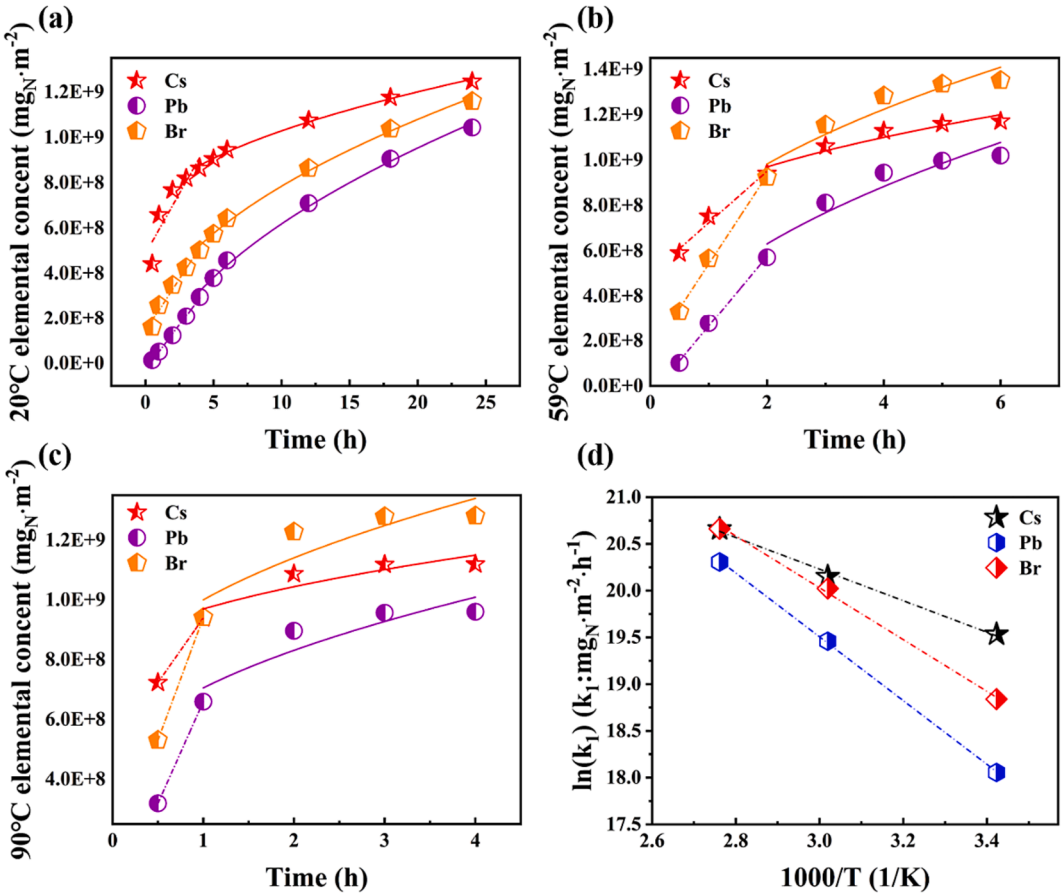

Fig. 8. Elemental release mass cumulative curves at 20 °C (a), 59 °C (b), and 90 °C (c). (d) Curve of ln(k_1) versus 1000/T (1/ Kelvin), where k_1 is the dissolution control rate constant in mg · m^{-2} · h^{-1} determined by the Cote's model.

stacking without grain boundaries, which might demonstrate superior stability to the polycrystalline structure [58]. Previous research by Al Jassim et al. revealed the degradation behavior of $MAPbI_3$ films and single crystals exposed to air by CL spectroscopy [56] and suggested higher phase stability of a single crystal than polycrystalline due to the more defects and grain boundaries of $MAPbI_3$ polycrystals, which can lead to severe phase degradation than single crystals. However, the $CsPbBr_3$ single crystals studied herein demonstrated severe phase degradation by water interaction, which could be attributed to the formation of pyramid-like vacancy defects and edge dislocations on the surface during the spontaneous growth of the single crystals, as previously observed in the SEM characterization of the single crystals in Fig. 2a-d. Liang et al. previously reported that $CsPbBr_3$ polycrystalline films can maintain stable performance in humid air (90%-95% RH, 25 °C) for more than 3 months [57], so the humidity stability of $CsPbBr_3$ single crystals in humid air must be further evaluated.

The presence of Cs^+ cations in the A-site of $CsPbBr_3$ single crystals makes them naturally more thermally stable compared with organic-inorganic hybrid perovskites, which has been favorably demonstrated in previous literature and in the current work [30,42]. Although hybrid perovskites have been found to achieve superior photoelectric conversion efficiencies [15], their MA^+ volatility leads to rapid thermal decomposition at relatively low temperatures. Bert Conings et al. [16] experimentally found that $MAPbI_3$ perovskites exhibit irreversible degradation behavior even in an inert atmosphere at 85 °C, which is detrimental to the stability of hybrid perovskites. The strong polarization of MA^+ also causes ion migration problems in light and thermal environments. Yuan et al. [17] discussed in detail the mechanism and means to eliminate the ion migration of $MAPbCl_3$ perovskites on the devices in their work. Currently, the replacement of organic-inorganic hybrid perovskites with all-inorganic perovskites $CsPbBr_3$ or the doping of inorganic cation Cs^+ into the A-site of hybrid perovskites to improve the performance and stability of hybrid perovskites is an interesting direction to scientists [58,59].

Therefore, the hydrolysis of the $CsPbBr_3$ single crystals is actually the result of the combined action of water, heat, and oxygen. Combined with the previous analysis, we reviewed the chemical dissolution process of single crystals. The step-wise phase decomposition and elemental dissolution behavior of $CsPbBr_3$ single crystals are proposed in Fig. 9 based on the following observation: the interaction between a water molecule and $CsPbBr_3$ single crystal leads to the preferential release of Cs and Br from the surface point defects and edge dislocations due to the relatively low dissolution activation energy (E_a) and weak bonding strength [55]. The continuous waste diffusion and penetration following the surface etching pits down to the center of the single crystal resulted in the sheet-like structure and porous alteration layer, as shown in the SEM images (Fig. 6b). Meanwhile, the preferential release of Cs and Br led to phase degradation, with the surface alteration layer being identified as $CsPb_2Br_5$, as confirmed by the XRD results (Fig. 4a, b). Further water molecule diffusion and reaction resulted in the phase decomposition of $CsPb_2Br_5$ into $PbBr_2$ and CsBr, with $PbBr_2$ diffusing and migrating out of the matrix to form a needle-like crystal structure of PbBr(OH) loosely packed on the surface. A simple mean square displacement (MSD) calculation by ab-initio first-principles has further been carried out for the aqueous corrosion of $CsPbBr_3$ single crystals, try to understanding the bonding strength of $CsPbBr_3$ (Fig. S3). Results indicate a higher MSD of Br^- and Cs^+ compared to Pb^{2+} over 6 ps and implies that the Br^- first separates, followed by Cs^+, and Pb^{2+} which is consistent with our experimentally results for the preferential release of Cs^+ and Br^-.

The corrosion degradation mechanism of $CsPbBr_3$ single crystals with the preferential release of Cs and Br ions obtained in this work would likely guide the stability regulation of this material. For example, the binding energy of Cs and Br in the lattice can be enhanced by artificially doping small radius or electronegative elements at the B-site and then achieve elemental reinforcement, such as in the work of Hu, Jitendra et al. [60,61]. In addition, specific elements can be incorporated in the perovskite to accelerate the in-situ formation of passivation film, similar to the metal oxide layers [50], thereby passivating the $CsPbBr_3$ surface. Organic molecules with hydrophobic properties can also be used to modify the surface of single crystals to enhance their resistance to humidity and slow down the corrosion of perovskite [62], which can accelerate the application of halide perovskite single crystal by increasing its phase stability.

6. Conclusions

In this study, the thermal and chemical stability of the $CsPbBr_3$ single crystals were thoroughly studied. Results demonstrated that the single crystal exhibited robust thermal stability without phase degradation observed at 460 °C. However, the single crystal started to melt at around 310 °C, which would affect the application of bulk single crystals above this temperature. The chemical degradation behavior of $CsPbBr_3$ single crystals under an aqueous environment was also studied by semi-dynamic leaching experiments. The water-induced phase degradation of $CsPbBr_3$ to $CsPb_2Br_5$ with the preferential release of Cs and Br elements was the main mechanism of phase degradation of $CsPbBr_3$ single crystals, which could be attributed to the low ionic bonding energy of Cs and Br ions in the lattice, as evidenced by their low dissolution activation energy. Moreover, surface point defects and edge dislocations of

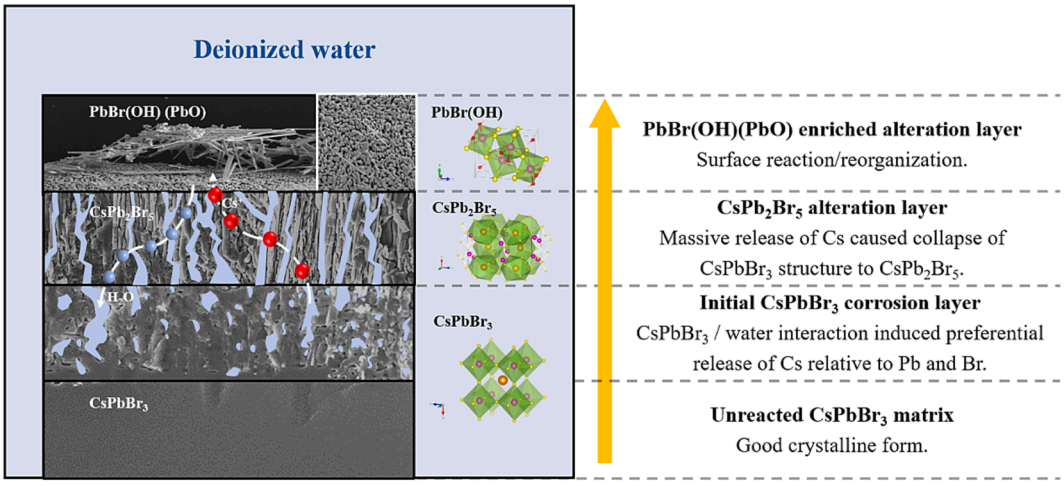

Fig. 9. Schematic mechanistic diagram to illustrate the stepwise phase degradation process of $CsPbBr_3$ single crystals in deionized water.

single crystals led to a rapid initial element release because of the high surface energy and chemical inhomogeneity of these sites. A step-wise single-crystal dissolution behavior was further revealed, which could guide the design of a single crystal through multiple scale strategies to enhance the stability of single-crystal applications.

Declaration of Competing Interest

The authors declare that they have no known competing financial interests or personal relationships that could have appeared to influence the work reported in this paper.

Data availability

Data will be made available on request.

Acknowledgements

The semi-dynamic leaching test of the single crystal $CsPbBr_3$ was supported by the Fund of Science and Technology on Reactor Fuel and Materials Laboratory [Grant number 6142A06070306]; The synthesis and characterization of the single crystal $CsPbBr_3$ was partially funded by the Fundamental Research Funds for the Central Universities [Grant number 1006-YAH22061] and the National Natural Science Foundation of China [Grant number 12275130].

We acknowledge the Center for Microscopy and Analysis at Nanjing University of Aeronautics and Astronautics for the technical assistance.

Appendix A. Supplementary data

Supplementary data to this article can be found online at https://doi.org/10.1016/j.cej.2023.146209.

References

[1] P.N. Luke, M. Amman, Room-temperature replacement for Ge detectors-are we there yet? IEEE Trans. Nucl. Sci. 54 (2007) 834–842, https://doi.org/10.1109/TNS.2007.903184.
[2] V.M. Zaletin, Development of semiconductor detectors based on wide-gap materials, At. Energ. 97 (2004) 773–780, https://doi.org/10.1007/s10512-005-0061-5.
[3] J.S. Iwanczyk, B.E. Patt, Y.J. Wang, A.K. Khusainov, Comparison of HgI_2, CdTe and Si (p-i-n) X-ray detectors, Nucl. Instruments Methods Phys. Res. Sect. A Accel. Spectrometers, Detect. Assoc. Equip. 380 (1996) 186–192, https://doi.org/10.1016/S0168-9002(96)00494-9.
[4] T.E. Schlesinger, J.E. Toney, H. Yoon, E.Y. Lee, B.A. Brunett, L. Franks, R.B. James, Cadmium zinc telluride and its use as a nuclear radiation detector material, Mater. Sci. Eng. R Reports. 32 (2001) 103–189, https://doi.org/10.1016/S0927-796X(01)00027-4.
[5] J.S. Iwanczyk, Y.J. Wang, J.G. Bradley, A.L. Albee, W.F. Schnepple, Advances in the development of encapsulants for mercuric iodide X-Ray detectors, IEEE Trans. Nucl. Sci. 37 (1990) 2214–2218, https://doi.org/10.1109/23.101259.
[6] C.C. Stoumpos, M.G. Kanatzidis, Halide perovskites: poor man's high-performance semiconductors, Adv. Mater. 28 (2016) 5778–5793, https://doi.org/10.1002/adma.201600265.
[7] S. Yakunin, M. Sytnyk, D. Kriegner, S. Shrestha, M. Richter, G.J. Matt, H. Azimi, C. J. Brabec, J. Stangl, M.V. Kovalenko, W. Heiss, Detection of X-ray photons by solution-processed lead halide perovskites, Nat. Photonics 9 (2015) 444–449, https://doi.org/10.1038/nphoton.2015.82.
[8] J. Kang, L.W. Wang, High defect tolerance in lead halide perovskite CsPbBr 3, J. Phys. Chem. Lett. 8 (2017) 489–493, https://doi.org/10.1021/acs.jpclett.6b02800.
[9] C.C. Stoumpos, C.D. Malliakas, M.G. Kanatzidis, Semiconducting tin and lead iodide perovskites with organic cations: Phase transitions, high mobilities, and near-infrared photoluminescent properties, Inorg. Chem. 52 (2013) 9019–9038, https://doi.org/10.1021/ic401215x.
[10] H. Wei, D. Desantis, W. Wei, Y. Deng, D. Guo, T.J. Savenije, L. Cao, J. Huang, Dopant compensation in alloyed $CH_3NH_3PbBr_{3-x}Cl_x$ perovskite single crystals for gamma-ray spectroscopy, Nat. Mater. 16 (2017) 826–833, https://doi.org/10.1038/nmat4927.
[11] H. Zhang, J.W. Lee, G. Nasti, R. Handy, A. Abate, M. Grätzel, N.G. Park, Lead immobilization for environmentally sustainable perovskite solar cells, Nature 617 (2023) 687–695, https://doi.org/10.1038/s41586-023-05938-4.
[12] W.-J. Yin, H. Chen, T. Shi, S.-H. Wei, Y. Yan, Origin of high electronic quality in structurally disordered $CH_3NH_3PbI_3$ and the passivation effect of Cl and O at grain boundaries, Adv. Electron. Mater. 1 (6) (2015) 1500044.
[13] O. Yaffe, Y. Guo, L.Z. Tan, D.A. Egger, T. Hull, C.C. Stoumpos, F. Zheng, T.F. Heinz, L. Kronik, M.G. Kanatzidis, J.S. Owen, A.M. Rappe, M.A. Pimenta, L.E. Brus, Local polar fluctuations in lead halide perovskite crystals, Phys. Rev. Lett. 118 (2017) 1–6, https://doi.org/10.1103/PhysRevLett.118.136001.
[14] J. Burschka, N. Pellet, S.J. Moon, R. Humphry-Baker, P. Gao, M.K. Nazeeruddin, M. Grätzel, Sequential deposition as a route to high-performance perovskite-sensitized solar cells, Nature 499 (2013) 316–319, https://doi.org/10.1038/nature12340.
[15] A. Polman, M. Knight, E.C. Garnett, B. Ehrler, W.C. Sinke, Photovoltaic materials: present efficiencies and future challenges, Science (80-.) (2016) 352, https://doi.org/10.1126/science.aad4424.
[16] B. Conings, J. Drijkoningen, N. Gauquelin, A. Babayigit, J. D'Haen, L. D'Olieslaeger, A. Ethirajan, J. Verbeeck, J. Manca, E. Mosconi, F. De Angelis, H. G. Boyen, Intrinsic thermal instability of methylammonium lead trihalide perovskite, Adv. Energy Mater. 5 (2015) 1–8, https://doi.org/10.1002/aenm.201500477.
[17] Y. Yuan, J. Huang, Ion migration in organometal trihalide perovskite and its impact on photovoltaic efficiency and stability, Acc. Chem. Res. 49 (2016) 286–293, https://doi.org/10.1021/acs.accounts.5b00420.
[18] F. Wang, H. Zhang, Q. Sun, A. Ben Hafsia, Z. Chen, B. Zhang, Y. Xu, W. Jie, Low-temperature solution growth and characterization of halogen (Cl, I)-doped $CsPbBr_3$ crystals, Cryst. Growth Des. 20 (2020) 1638–1645, https://doi.org/10.1021/acs.cgd.9b01368.
[19] M.I. Saidaminov, M.A. Haque, J. Almutlaq, S. Sarmah, X.H. Miao, R. Begum, A. A. Zhumekenov, I. Dursun, N. Cho, B. Murali, O.F. Mohammed, T. Wu, O.M. Bakr, Inorganic lead halide perovskite single crystals: phase-selective low-temperature growth, carrier transport properties, and self-powered photodetection, Adv. Opt. Mater. 5 (2017), https://doi.org/10.1002/adom.201600704.
[20] Y. He, L. Matei, H.J. Jung, K.M. McCall, M. Chen, C.C. Stoumpos, Z. Liu, J. A. Peters, D.Y. Chung, B.W. Wessels, M.R. Wasielewski, V.P. Dravid, A. Burger, M. G. Kanatzidis, High spectral resolution of gamma-rays at room temperature by perovskite $CsPbBr_3$ single crystals, Nat. Commun. 9 (2018) 1–8, https://doi.org/10.1038/s41467-018-04073-3.
[21] Y. He, M. Petryk, Z. Liu, D.G. Chica, I. Hadar, C. Leak, W. Ke, I. Spanopoulos, W. Lin, D.Y. Chung, B.W. Wessels, Z. He, M.G. Kanatzidis, $CsPbBr_3$ perovskite detectors with 1.4% energy resolution for high-energy γ-rays, Nat. Photonics 15 (2021) 36–42, https://doi.org/10.1038/s41566-020-00727-1.
[22] J. Shamsi, A.S. Urban, M. Imran, L. De Trizio, L. Manna, Metal halide perovskite nanocrystals: synthesis, post-synthesis modifications, and their optical properties, Chem. Rev. 119 (2019) 3296–3348, https://doi.org/10.1021/acs.chemrev.8b00644.
[23] C. Caddeo, M.I. Saba, S. Meloni, A. Filippetti, A. Mattoni, Collective molecular mechanisms in the $CH_3NH_3PbI_3$ dissolution by liquid water, ACS Nano 11 (2017) 9183–9190, https://doi.org/10.1021/acsnano.7b04116.
[24] E. Mosconi, J.M. Azpiroz, F. De Angelis, Ab initio molecular dynamics simulations of methylammonium lead iodide perovskite degradation by water, Chem. Mater. 27 (2015) 4885–4892, https://doi.org/10.1021/acs.chemmater.5b01991.
[25] K. Bryce, K. Yang, Y. Wang, J. Lian, Chemical durability and degradation mechanisms of $CsPbI_3$ as a potential host phase for cesium and iodine sequestration, RSC Adv. 12 (2022) 12242–12252, https://doi.org/10.1039/d2ra01259f.
[26] C. Zheng, O. Rubel, Unraveling the water degradation mechanism of $CH_3NH_3PbI_3$, J. Phys. Chem. C 123 (2019) 19385–19394, https://doi.org/10.1021/acs.jpcc.9b05516.
[27] J. Peng, C.Q. Xia, Y. Xu, R. Li, L. Cui, J.K. Clegg, L.M. Herz, M.B. Johnston, Q. Lin, Crystallization of $CsPbBr_3$ single crystals in water for X-ray detection, Nat. Commun. 12 (2021) 1–10, https://doi.org/10.1038/s41467-021-21805-0.
[28] J.H. ter Horst, C. Schmidt, J. Ulrich, Fundamentals of industrial crystallization, Second Edi Elsevier B.V. (2015), https://doi.org/10.1016/B978-0-444-63303-3.00032-8.
[29] H. Zhang, X. Liu, J. Dong, H. Yu, C. Zhou, B. Zhang, Y. Xu, W. Jie, Centimeter-sized inorganic lead halide perovskite $CsPbBr_3$ crystals grown by an improved solution method, Cryst. Growth Des. 17 (2017) 6426–6431, https://doi.org/10.1021/acs.cgd.7b01086.
[30] Y. Liu, Z. Yang, D. Cui, X. Ren, J. Sun, X. Liu, J. Zhang, Q. Wei, H. Fan, F. Yu, X. Zhang, C. Zhao, S. Liu, Two-Inch-sized perovskite $CH_3NH_3PbX_3$ (X = Cl, Br, I) Crystals: growth and characterization, Adv. Mater. 27 (2015) 5176–5183, https://doi.org/10.1002/adma.201502597.
[31] K. Yang, W. Zhu, S. Scott, Y. Wang, J. Wang, B.J. Riley, J. Vienna, J. Lian, Immobilization of cesium and iodine into $Cs_3Bi_2I_9$ perovskite-silica composites and core-shell waste forms with high waste loadings and chemical durability, J. Hazard. Mater. 401 (2021), 123279, https://doi.org/10.1016/j.jhazmat.2020.123279.
[32] P.R. Sahm, I. Egry, T. Volkmann, Schmelze, erstarrung, grenzflächen: eine einführung in die physik und technologie flüssiger und fester metalle, springer-verlag, Berlin Heidelberg (1999), https://doi.org/10.1007/978-3-642-58523-4.
[33] C.C. Stoumpos, C.D. Malliakas, J.A. Peters, Z. Liu, M. Sebastian, J. Im, T. C. Chasapis, A.C. Wibowo, D.Y. Chung, A.J. Freeman, B.W. Wessels, M. G. Kanatzidis, Crystal growth of the perovskite semiconductor CsPbBr 3: a new material for high-energy radiation detection, Cryst. Growth Des. 13 (2013) 2722–2727, https://doi.org/10.1021/cg400645t.
[34] V.E. Distanov, V.A. Drebushchak, Melting of $PbBr_2$. A DSC investigation, J. Therm. Anal. Calorim. 57 (1999) 599–605, https://doi.org/10.1023/a:1010105100283.

[35] Z. Ahmad, A. Mishra, Growth of $PbBr_2$ microrods with unique structure and surface morphology, J. Mater. Sci. Mater. Electron. 31 (2020) 4672–4676, https://doi.org/10.1007/s10854-020-03019-0.
[36] P. Sujith, M. Pratheek, S.R. Parne, P. Predeep, Growth and characterization of high-quality orthorhombic phase $CsPbBr_3$ perovskite single crystals for optoelectronic applications, J. Electron. Mater. 52 (2023) 718–729, https://doi.org/10.1007/s11664-022-10042-w.
[37] S. Das Adhikari, S. Masi, C. Echeverría-Arrondo, S. Miralles-Comins, R.S. Sánchez, J.A. Fernandes, V. Chirvony, J.P. Martínez-Pastor, V. Sans, I. Mora-Seró, Continuous-flow synthesis of orange emitting Sn(II)-doped CsBr materials, Adv. Opt. Mater. 9 (2021), https://doi.org/10.1002/adom.202101024.
[38] M. Liao, B. Shan, M. Li, In Situ raman spectroscopic studies of thermal stability of all-inorganic cesium lead halide ($CsPbX_3$, X = Cl, Br, I) perovskite nanocrystals, J. Phys. Chem. Lett. 10 (2019) 1217–1225, https://doi.org/10.1021/acs.jpclett.9b00344.
[39] Z. Qin, S. Dai, V.G. Hadjiev, C. Wang, L. Xie, Y. Ni, C. Wu, G. Yang, S. Chen, L. Deng, Q. Yu, G. Feng, Z.M. Wang, J. Bao, Revealing the origin of luminescence center in 0D Cs_4PbBr_6 perovskite, Chem. Mater. 31 (21) (2019) 9098–9104.
[40] A. You, M.A.Y. Be, I. In, Identification of the symmetry of phonon modes in in phase IV by Raman and resonance-Raman scattering, J. Appl. Phys. (1997) 5391–5395, https://doi.org/10.1063/1.366307.
[41] W. Du, S. Zhang, Z. Wu, Q. Shang, Y. Mi, J. Chen, C. Qin, X. Qiu, Q. Zhang, X. Liu, Unveiling lasing mechanism in $CsPbBr_3$ microsphere cavities, Nanoscale 11 (2019) 3138–3144, https://doi.org/10.1039/c8nr09634a.
[42] S. Gholipour, M. Saliba, From exceptional properties to stability challenges of perovskite solar cells, Small 14 (2018) 1–10, https://doi.org/10.1002/smll.201802385.
[43] V.G. Hadjiev, C. Wang, Y. Wang, X. Su, H.A. Calderon, F. Robles Hernandez, Z. M. Wang, J.M. Bao, Phonon fingerprints of $CsPb_2Br_5$, J. Phys. Condens. Matter 30 (40) (2018), 405703, https://doi.org/10.1088/1361-648X/aadeb4.
[44] P. Shen, X. Ma, F. Pan, Y.N. Wang, B. Liu, H. Ye, Extrinsic photoluminescence and resonant raman spectra of $CsPb_2Br_5$ microspheres, J. Phys. Chem. C 125 (2021) 6767–6772, https://doi.org/10.1021/acs.jpcc.0c11301.
[45] E.S. Reid, R.P. Cooney, P.J. Hendra, M. Fleischmann, A Raman Spectroscopic Study of Corrosion of Lead Electrodes in Aqueous Chloride Media, 80 (1977) 405–408. https://doi.org/10.1016/S0022-0728(77)80063-6.
[46] D.U. Wiechert, S.P. Grabowski, M. Simon, Raman spectroscopic investigation of evaporated PbO layers, Thin Solid Films 484 (2005) 73–82, https://doi.org/10.1016/j.tsf.2005.02.010.
[47] P. Tsai, R.P. Cooney, Raman spectra of polynuclear hydroxo-compounds of lead(II) chloride, J. Chem. Soc. Dalt. Trans. (16) (1976) 1631.
[48] H. Sadeghzadeh, A. Morsali, V.T. Yilmaz, O. Büyükgüngör, Sonochemical synthesis of nano-scale mixed-ligands lead(II) coordination polymers as precursors for preparation of PbO and PbBr(OH) nano-structures; thermal, structural and X-ray powder diffraction studies, Ultrason. Sonochem. 17 (2010) 592–597, https://doi.org/10.1016/j.ultsonch.2009.11.015.
[49] W. Wang, Y. Yu, S. Attique, J. Hou, F. Jun, Y. Xie, L. Mao, X. Yu, X. Zhang, S. Wang, C. Wu, B. Cao, S. Yang, Sustainable fabrication of ultralong Pb(OH)Br nanowires and their conversion to luminescent $CH_3NH_3PbBr_3$ nanowires, Green Chem. 23 (2021) 7956–7962, https://doi.org/10.1039/d1gc02073k.
[50] G.S. Frankel, J.D. Vienna, J. Lian, J.R. Scully, S. Gin, J.V. Ryan, J. Wang, S.H. Kim, W. Windl, J. Du, A comparative review of the aqueous corrosion of glasses, crystalline ceramics, and metals, npj Mater. Degrad. 2 (2018), https://doi.org/10.1038/s41529-018-0037-2.
[51] A. Lüttge, Crystal dissolution kinetics and Gibbs free energy, J. Electron Spectros. Relat. Phenomena. 150 (2006) 248–259, https://doi.org/10.1016/j.elspec.2005.06.007.
[52] A.C. Lasaga, A. Luttge, Variation of crystal dissolution rate based on a dissolution stepwave model, Science 291 (2001) 2400–2404, https://doi.org/10.1126/science.1058173.
[53] P.L. Côté, T.W. Constable, A. Moreira, An evaluation of cement-based waste forms using the results of approximately two years of dynamic leaching, Nucl. Chem. Waste Manag. 7 (1987) 129–139, https://doi.org/10.1016/0191-815X(87)90007-6.
[54] E.L. Cussler, Permeability properties of plastics and elastomers, J. Control. Release 92 (2003) 399, https://doi.org/10.1016/s0168-3659(03)00333-x.
[55] S. Meloni, T. Moehl, W. Tress, M. Franckeviius, M. Saliba, Y.H. Lee, P. Gao, M. K. Nazeeruddin, S.M. Zakeeruddin, U. Rothlisberger, M. Graetzel, Ionic polarization-induced current-voltage hysteresis in $CH_3NH_3PbX_3$ perovskite solar cells, Nat. Commun. 7 (2016), https://doi.org/10.1038/ncomms10334.
[56] C. Xiao, Z. Li, H. Guthrey, J. Moseley, Y. Yang, S. Wozny, H. Moutinho, B. To, J. J. Berry, B. Gorman, Y. Yan, K. Zhu, M. Al-Jassim, Mechanisms of electron-beam-induced damage in perovskite thin films revealed by cathodoluminescence spectroscopy, J. Phys. Chem. C 119 (2015) 26904–26911, https://doi.org/10.1021/acs.jpcc.5b09698.
[57] J. Liang, C. Wang, Y. Wang, Z. Xu, Z. Lu, Y. Ma, H. Zhu, Y. Hu, C. Xiao, X. Yi, G. Zhu, H. Lv, L. Ma, T. Chen, Z. Tie, Z. Jin, J. Liu, All-inorganic perovskite solar cells, J. Am. Chem. Soc. 138 (2016) 15829–15832, https://doi.org/10.1021/jacs.6b10227.
[58] J. Ding, S. Du, T. Zhou, Y. Yuan, X. Cheng, L. Jing, Q. Yao, J. Zhang, Q. He, H. Cui, X. Zhan, H. Sun, Cesium decreases defect density and enhances optoelectronic properties of mixed $MA_{1-x}Cs_xPbBr_3$ single crystal, J. Phys. Chem. C 123 (2019) 14969–14975, https://doi.org/10.1021/acs.jpcc.9b03987.
[59] Y. Li, J. Duan, H. Yuan, Y. Zhao, B. He, Q. Tang, Lattice modulation of alkali metal cations doped $Cs_{1-x}R_xPbBr_3$ halides for inorganic perovskite solar cells, Sol. RRL. 2 (2018) 1–8, https://doi.org/10.1002/solr.201800164.
[60] Y. Hu, F. Bai, X. Liu, Q. Ji, X. Miao, T. Qiu, S. Zhang, Bismuth incorporation stabilized α-$CsPbI_3$ for Fully inorganic perovskite solar cells, ACS Energy Lett. 2 (10) (2017) 2219–2227.
[61] J. Bahadur, A.H. Ghahremani, S. Gupta, T. Druffel, M.K. Sunkara, K. Pal, Enhanced moisture stability of $MAPbI_3$ perovskite solar cells through Barium doping, Sol. Energy 190 (2019) 396–404, https://doi.org/10.1016/j.solener.2019.08.033.
[62] S. Yang, Y. Wang, P. Liu, Y.B. Cheng, H.J. Zhao, H.G. Yang, Functionalization of perovskite thin films with moisture-tolerant molecules, Nat. Energy 1 (2016) 1–7, https://doi.org/10.1038/NENERGY.2015.16.